APL Quantum

RESEARCH ARTICLE | JUNE 04 2025

Origin of performance enhancement of superconducting nanowire single-photon detectors by He-ion irradiation

Stefan Strohauer ; Fabian Wietschorke ; Markus Döblinger ; Christian Schmid ; Stefanie Grotowski ; Lucio Zugliani ; Björn Jonas ; Kai Müller ; Jonathan J. Finley

APL Quantum 2, 026131 (2025)
https://doi.org/10.1063/5.0259935

Origin of performance enhancement of superconducting nanowire single-photon detectors by He-ion irradiation

Cite as: APL Quantum 2, 026131 (2025); doi: 10.1063/5.0259935
Submitted: 21 January 2025 • Accepted: 20 May 2025 •
Published Online: 4 June 2025

Stefan Strohauer,[1,2,a)] Fabian Wietschorke,[1,3] Markus Döblinger,[4] Christian Schmid,[1,3] Stefanie Grotowski,[1,2] Lucio Zugliani,[1,3] Björn Jonas,[1,3] Kai Müller,[1,3,5] and Jonathan J. Finley[1,2,5,b)]

AFFILIATIONS

[1] Walter Schottky Institute, Technical University of Munich, 85748 Garching, Germany
[2] TUM School of Natural Sciences, Technical University of Munich, 85748 Garching, Germany
[3] TUM School of Computation, Information and Technology, Technical University of Munich, 80333 Munich, Germany
[4] Faculty for Chemistry and Pharmacy, Ludwig Maximilian University of Munich, 81377 Munich, Germany
[5] Munich Center for Quantum Science and Technology (MCQST), 80799 Munich, Germany

[a)] **Author to whom correspondence should be addressed:** stefan.strohauer@tum.de
[b)] **E-mail:** jj.finley@tum.de

ABSTRACT

Superconducting nanowire single-photon detectors (SNSPDs) are indispensable in fields such as quantum science and technology, astronomy, and biomedical imaging, where high detection efficiency, low dark count rates, and high timing accuracy are required. Recently, helium (He) ion irradiation was shown to be a promising method to enhance SNSPD performance. Here, we study how changes in the underlying superconducting NbTiN film and the SiO_2/Si substrate affect device performance. While irradiated and unirradiated NbTiN films show similar crystallinity, we observe He bubble formation below the SiO_2/Si interface and an amorphization of the Si substrate. Both reduce the thermal conductance between the superconducting thin film and the substrate from 210 to 70 W m^{-2} K^{-4} after irradiation with 2000 ions nm^{-2}. This effect, combined with the lateral straggle of He ions in the substrate, allows the modification of the superconductor-to-substrate thermal conductance of an SNSPD by selectively irradiating only the regions around the nanowire. With this approach, we achieved a broader bias current range (9.8 μA vs 3.7 μA) in which the detector operates at its maximum detection efficiency, which is beneficial for reducing dark counts while maintaining high sensitivity. Moreover, the photon-assisted critical current remained similar to that of the unirradiated reference device (59.0 μA vs 60.1 μA), while full irradiation reduced it to 22.4 μA. Our results suggest that the irradiation-induced reduction of the thermal conductance significantly enhances SNSPD sensitivity, offering a novel approach to locally engineer substrate properties for improved detector performance.

I. INTRODUCTION

Superconducting nanowire single-photon detectors (SNSPDs)[1] play an increasing role in a multitude of fields such as quantum science and technology,[2–9] optical communication,[10,11] astronomy,[12] biology,[13–15] and medicine.[16–18] With their near-unity efficiency,[19,20] subhertz dark count rate,[21] picosecond timing jitter,[22] and typically nanosecond reset times (with records as low as 130 ps[23]), they are ideally suited for demanding applications such as photonic quantum computing,[24] lidar,[22,25–27] particle and dark matter detection,[28–32] or infrared fluorescence microscopy for *in vivo* deep brain imaging.[13–15] He ion irradiation has emerged as a powerful technique for further enhancing SNSPD performance across multiple metrics.[33–37] It systematically alters properties of the underlying superconducting films by creating defects, increasing sheet resistance, and decreasing the critical temperature of NbN, NbTiN, and

MgB_2 superconducting thin films.[34–38] This effect has been successfully applied not only as a post-processing technique to SNSPDs but also to fabricate Josephson junctions[38] and for direct-write modification without requiring etching steps.[39] Since the critical temperature is directly proportional to the superconducting energy gap, the reduction due to He ion irradiation results in enhanced sensitivity to single photons, directly improving the detection efficiency.[34] In addition, several indirect benefits have been demonstrated: (1) lower dark count rates achieved by enabling operation at a lower percentage of the switching current while maintaining high detection efficiency;[33] (2) higher switching currents and pulse amplitudes for irradiated thick-film SNSPDs,[35] which typically correlate with reduced timing jitter;[40] and (3) the ability to individually tune detector properties to achieve uniform performance across arrays.[35] In addition to altering the superconducting properties of the film through defect creation, He ion irradiation can also modify the underlying substrate. Charaev *et al.*[36] observed that for their MgB_2-based single-photon detectors, He ion irradiation not only introduces defects in the superconducting film but also amorphizes the underlying SiC substrate, likely affecting the thermal conductance between the superconducting thin film and the substrate. This could lead to a prolonged lifetime of the normal conducting domain, thereby increasing the detection probability. However, it has remained unclear whether such mechanisms, in addition to irradiation-induced defect formation, play a significant role in the improved performance after irradiation.[36,37] In this work, we investigate how He ion irradiation modifies the morphology of both the NbTiN film and the SiO_2/Si substrate and discuss mechanisms by which these changes influence detector performance.

II. IRRADIATION-INDUCED CHANGES OF FILM AND SUBSTRATE MORPHOLOGY

To explore how He ion irradiation influences superconducting film and substrate morphology in this section, we fabricated nominally 12 nm thick NbTiN films via DC reactive magnetron sputtering onto SiO_2/Si substrates with a nominally 130 nm thick thermally grown SiO_2 layer. This relatively thick film was chosen to maximize the visibility of potential structural changes. Transmission electron microscopy (TEM) measurements later revealed these films have an actual thickness of (11.3 ± 0.5) nm. For the SNSPD measurements and thermal conductance studies presented in Secs. III and IV, we fabricated separate devices using thinner 8 nm thick NbTiN films, as thinner films provide the single-photon sensitivity necessary for reasonable detection efficiency measurements.[35] These 8 nm thick nanowires were used consistently across all electrical characterization and photon detection experiments throughout this work. We irradiated selected areas of both sample types with various fluences of 30 kV He ions before characterizing the 12 nm films using transmission electron microscopy (TEM) and atomic force microscopy (AFM). Figure 1 shows high-angle annular dark-field scanning transmission electron microscopy (HAADF-STEM) images of the stack NbTiN/SiO_2/Si in its unirradiated form and after irradiation with 500 and 2000 ions nm^{-2} (corresponding to 5×10^{16} and 2×10^{17} ions cm^{-2}). Following He ion irradiation, we observe that the Si substrate becomes amorphous and contains He bubbles (nano-sized voids filled with high-pressure He gas) in a region extending from the SiO_2/Si interface at 150 to ~340 nm depth, consistent with previous studies.[41–45]

This finding agrees with Monte Carlo simulations for the same NbTiN/SiO_2/Si stack, performed with the Stopping and Range of Ions in Matter (SRIM) 2008 software.[46] Figures 2(a)–2(c) show the calculated lateral and depth-resolved probability density function $f_{\text{area}}(x,z)$ of stopping positions of the He ions originating from the focused beam of a He ion microscope, as well as the depth-resolved FWHM of the lateral Gaussian distribution, and the probability density function $f_{\text{line}}(z)$ of He ions stopping at a certain depth z. The lateral distribution was calculated by projecting the three-dimensional stopping positions of He ions onto a plane perpendicular to the surface. Most of the He ions penetrate deep into the substrate before they stop, with the maximum of the distribution of implanted He ions at a depth of 335 nm, which is in the range where we observe He bubble formation. At the same time, the He distribution is broadened laterally and in depth due to scattering and recoil events. Therefore, the simulated lateral Gaussian distribution has a FWHM of 266 nm when considering all He ion stopping positions, 241 nm for the layer where most He ions stop, and 400 nm within the NbTiN layer (although the fraction of ions that stop within each nm of this layer is more than an order of magnitude smaller than deep in the substrate).

As mentioned above, the HAADF-STEM images in Fig. 1 reveal that He ion irradiation with 500 ions nm^{-2} (2000 ions nm^{-2}) transforms crystalline Si into an amorphous and porous structure with He bubbles. This extends to a depth of 105 nm (190 nm) below the SiO_2/Si interface, corresponding to a total depth of 255 nm (340 nm). Interestingly, the Si layer near the SiO_2/Si interface remains partially crystalline after irradiation with 500 ions nm^{-2} (see Appendix B), while for the higher fluence of 2000 ions nm^{-2}, the amorphous region extends all the way to the SiO_2–Si interface. The thickness of the SiO_2 layer, however, remains unchanged at (137 ± 3) nm after irradiation. As shown in Fig. 2(e), complementary HAADF-STEM imaging and energy-dispersive x-ray spectroscopy (EDX) of the amorphous Si region reveal that areas of dark contrast correspond to reduced Si content. These dark contrasts, originating from local minima in the projected Si thickness, are associated with He bubble formation during irradiation. This interpretation is supported by the irradiation-induced surface elevation of the stack measured by AFM, as discussed later in this section. To quantify these observations, we analyzed the spatial distribution of dark contrast in the amorphous Si region in Fig. 2(d). At each depth, we calculated the dark contrast area fraction by identifying regions below a threshold value after local background subtraction. This analysis shows that both the area fraction and average size of dark contrast regions reach their maxima at ~300 nm depth, closely matching the simulated peak of He ion stopping positions at 335 nm shown in Fig. 2(c). We observe these dark contrast regions in a range extending from approximately the SiO_2/Si interface (located at 150 nm depth) to about 340 nm depth. While the projective nature of TEM imaging prevents direct interpretation of individual feature sizes, this spatial correlation between dark contrast regions and simulated ion stopping positions, combined with the observed surface elevation in AFM measurements, indicates the formation of He bubbles in the Si substrate, consistent with previous studies.[41–45] Moreover, the NbTiN film exhibits increased wrinkling at higher He ion fluences, while it maintains its original thickness of (11.3 ± 0.5) nm and shows no visible cracks or noticeable material loss from sputtering. We use the term "wrinkling" rather than "surface

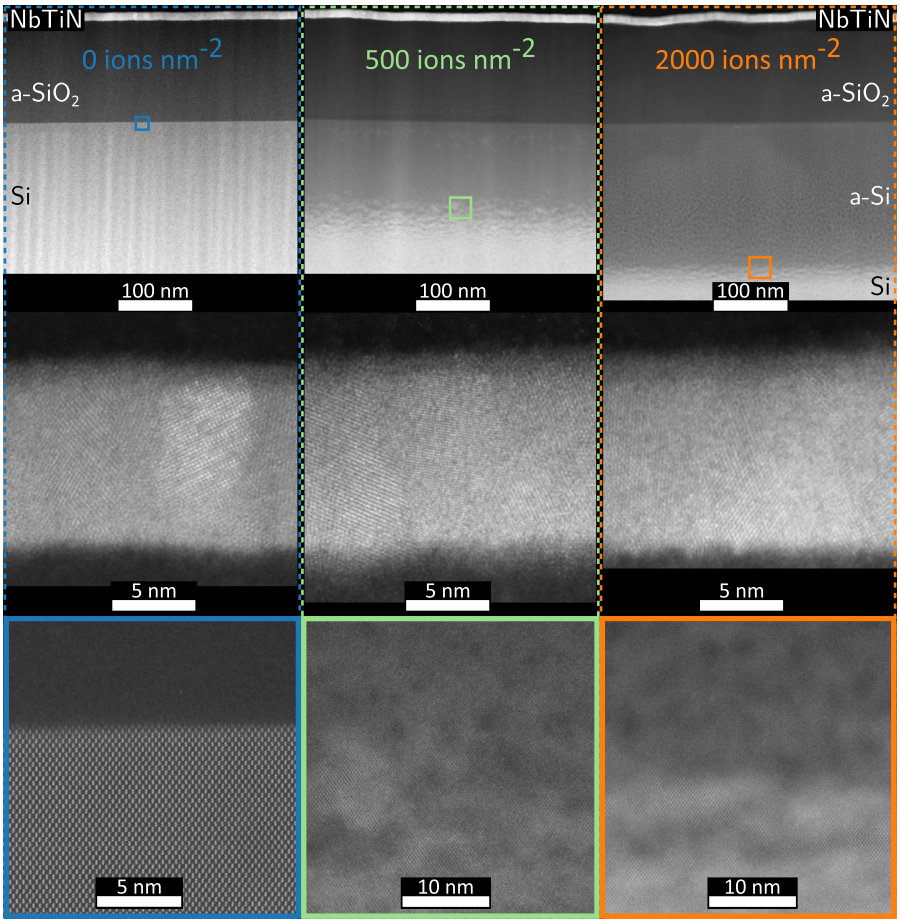

FIG. 1. HAADF-STEM images of $NbTiN/SiO_2/Si$ stacks before and after He ion irradiation: unirradiated (left column), irradiated with 500 ions nm^{-2} (middle column), and 2000 ions nm^{-2} (right column). Top row: Overview images showing the NbTiN film (light gray), the amorphous SiO_2 (dark gray), and the Si substrate. In the irradiated samples, the upper Si regions become amorphous (a-Si) with grayscale variations indicating porosity. The crystalline Si appears light gray. Middle row: High-resolution images of the NbTiN films reveal a similar thickness of 11.3 nm, 5 nm wide columnar δ-NbTiN domains, and a 1.5 nm thick amorphous oxygen-rich surface layer across all samples. Bottom row: Transition regions between amorphous and crystalline Si (locations marked by colored rectangles in the top row). The crystalline-amorphous interface coincides with the SiO_2/Si interface in the unirradiated sample, but lies 105 and 190 nm below the SiO_2/Si interface for the samples irradiated with 500 and 2000 ions nm^{-2}, respectively. Dark contrasts in the amorphous Si regions are associated with pores.

roughness" because the film undergoes a characteristic deformation where both its top and bottom surfaces exhibit synchronized undulations while maintaining constant thickness. This wrinkling and its correlation with AFM surface roughness measurements are analyzed in detail in Appendix C. Notably, despite the wrinkling of the NbTiN layer, the SiO_2/Si interface remains flat. Furthermore, at all fluences, the NbTiN film retains its columnar crystalline domains (NaCl-type face-centered cubic δ-phase of NbTiN) with an oxygen-rich top layer (see Appendix D for the elemental composition).[47–49] We do not see any substantial change in crystallinity or visible defects between the differently irradiated NbTiN films. This is surprising, since we expected the polycrystalline structure of the pristine NbTiN film to become more amorphous and exhibit an increasing number of defects with increasing He ion fluence.

In addition to the TEM characterization, the irradiated surfaces are investigated using an AFM (Bruker Dimension Icon) to gain information about the surface morphology and to compare it to the TEM measurements. Figure 3(a) shows the surface of an irradiated $4 \times 4\ \mu m^2$ NbTiN square. Upon irradiation with 2000 ions nm^{-2}, we observe a surface elevation of 28 nm and an increased surface roughness within the irradiated area. The elevation predominantly stems from He bubble formation in the silicon, as the density difference between amorphous and crystalline silicon is only 1.8%.[50] The topography also reveals uneven features at the edges of the irradiated area due to the He ion beam's rastering pattern, which scans each line right to left while progressing top to bottom. Since the upper and right edges are the starting points of this scanning pattern, this results in greater accumulation of redeposited material at these edges.[51,52] To quantify the dependence of the surface elevation and the surface roughness on the He ion fluence, we performed AFM measurements for multiple fluences and not only for the $NbTiN/SiO_2/Si$ stack but also for two reference stacks, $Au/SiO_2/Si$ and SiO_2/Si. Figure 3(b) shows height profiles across the center of three differently irradiated $NbTiN/SiO_2/Si$ stacks. Each point represents the average height over a 1.5 μm wide strip in the y-direction (128 AFM scan lines), perpendicular to the profile direction shown in Fig. 3(a). As shown in Fig. 3(c), the surface elevation increases linearly with the He ion fluence for both Au and NbTiN thin films, as well as for the bare SiO_2/Si substrate. This behavior is consistent with expectations, since most He ions interact only weakly with the film and stop deep inside the substrate where they form He bubbles

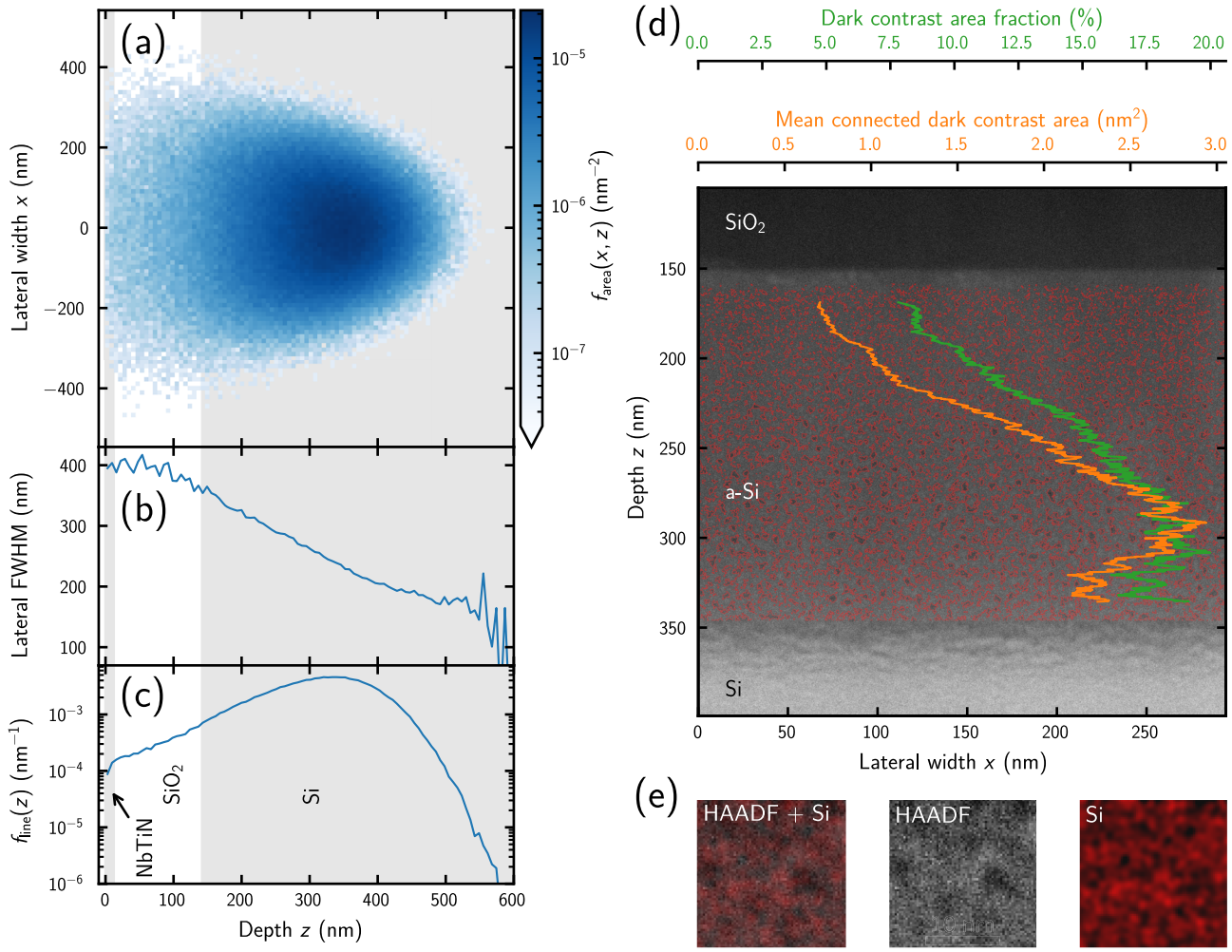

FIG. 2. Simulated distribution of He ion stopping positions (a)–(c) and experimental analysis of structural modifications (d) and (e) in the irradiated NbTiN/SiO_2/Si stack. (a) Lateral and depth-resolved probability density function $f_{area}(x,z)$ of the stopping positions. (b) Depth-resolved FWHM of the lateral Gaussian distribution. (c) Probability density function $f_{line}(z)$ for He ions stopping at a certain depth z. (d) HAADF-STEM image of the sample irradiated with 2000 ions nm^{-2}, with dark contrast regions highlighted by red outlines. Overlaid curves show the dark contrast area fraction (green) and average size of connected dark contrast regions (orange) vs depth z. (e) High-magnification comparison of HAADF contrast with Si content: overlay of HAADF and Si EDX signal (left), HAADF image (center), and Si EDX map (right), demonstrating the correlation between dark HAADF contrast and reduced Si content.

that cause the surface to rise. The linear fit (excluding fluences below 250 ions nm^{-2}) has a non-zero intercept at 120 ions nm^{-2}, from which we conclude that significant bubble formation and surface elevation begin just above a certain fluence, similar to an observation in Ref. 53. To study the dependence of the root mean square (rms) roughness of irradiated NbTiN films on the He ion fluence, we irradiated squares with dimensions of 4 × 4 and 15 × 15 μm^2 with beam currents ranging from 10.6 to 119 pA, which were chosen to obtain irradiation times between 1 and 10 min even for the highest fluences. As shown in Fig. 3(d), the surface roughness of the NbTiN film increases from 0.43 nm for the unirradiated film to 1.85 nm at 1500 ions nm^{-2}. On the contrary, the bare SiO_2/Si substrate and the sample with a 10 nm gold layer do not show a systematic increase in roughness after irradiation (0.31 and 0.72 nm average roughness, respectively). Moreover, while the different squares of 4 × 4 and 15 × 15 μm^2 exhibit similar roughness in the homogeneously irradiated center regions, we observed a slightly higher surface roughness for higher beam currents as discussed in more detail in Appendix F. Furthermore, the surface roughness observed in the AFM measurements of this section correlates with the wrinkling identified in the TEM images above. This relationship is analyzed in detail in Appendix C.

Measurements in the literature have shown that ion irradiation enables plastic flow in SiO_2 and Si,[43,54–57] and that sputtered NbTiN typically exhibits internal stress.[58–62] This agrees with our observation of increasing wrinkling of the NbTiN film with increasing He

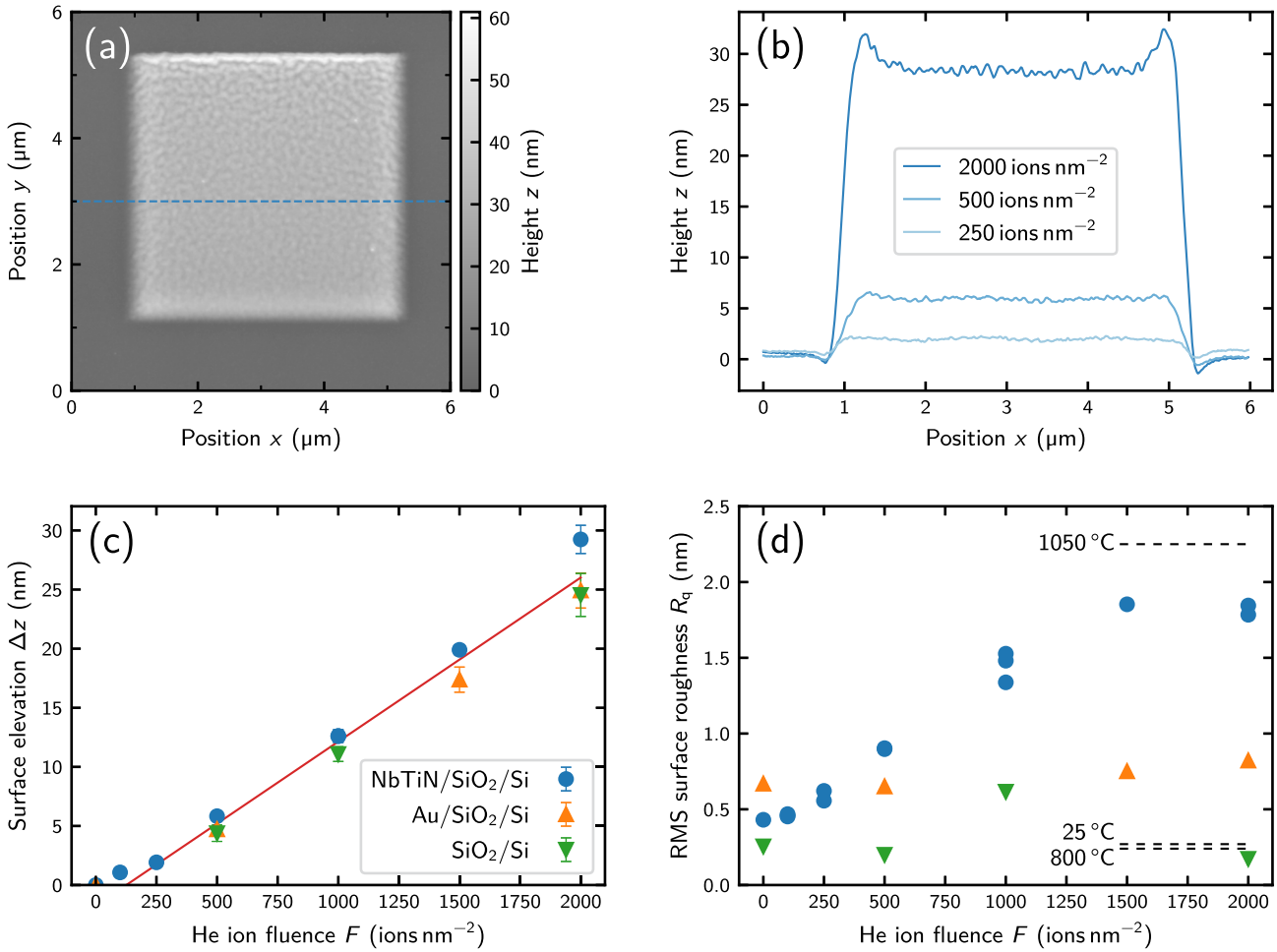

FIG. 3. AFM characterization of irradiated NbTiN films. (a) A representative square structure obtained after irradiation with 2000 ions nm^{-2}. (b) Line profiles for three different He ion fluences. For 2000 ions nm^{-2}, the profile is also indicated as a blue dashed line in (a). (c) The fluence-dependent surface elevation (mean height) of the quasi-flat center region of each irradiated area, extracted from profiles like those shown in (b). In addition to the stack NbTiN/SiO_2/Si, it was also measured for the reference stacks Au/SiO_2/Si and SiO_2/Si. The red line is a linear fit of all data with a fluence of 250 ions nm^{-2} or above. (d) Dependence of the rms surface roughness on the He ion fluence for the same stacks as in (c). The dashed lines show the measured roughness before and after annealing a second NbTiN/SiO_2/Si sample at temperatures of 800 and 1050 °C (see Appendix E for details).

ion fluence: When irradiating the NbTiN/SiO_2/Si stack, the stress in the NbTiN film can relax and deform the originally flat NbTiN film due to radiation-induced plastic flow of the underlying SiO_2. To test this hypothesis, we took a NbTiN film on a SiO_2/Si substrate of the same sputtering run and heated it to temperatures up to 1050 °C. Since the viscous flow of thermally grown SiO_2 starts at 960 °C,[63] we expected an increase in the NbTiN film wrinkling just above that temperature. Indeed, AFM line profiles do not differ between the original sample and the sample after heating it to 800 °C. However, after heating the sample to 1050 °C, it shows a substantial increase in wrinkling with the rms roughness increasing from 0.27 to 2.25 nm (more details in Appendix E). This observation indicates that stress in the NbTiN film is already present after sputtering and that it relaxes upon activating viscous flow of the underlying substrate. To verify that the deformation does not originate from strain in the substrate material, we also obtained reference data by irradiating the unprocessed wafer (SiO_2/Si stack) and the wafer with an evaporated gold layer on top. Both do not show an increase in wrinkling/roughness with increasing He ion fluence, as can be seen in Fig. 3(d).

In summary, we observe increased wrinkling of the NbTiN film as the He ion fluence increases, while its thickness and roughness remain unchanged. This wrinkling originates from relaxation of stress that builds up in the NbTiN film already during the sputtering process. When the NbTiN/SiO_2/Si stack is irradiated with He ions or heated to temperatures above 960 °C, viscous flow of the SiO_2 allows stress in the NbTiN layer to be released, causing the NbTiN to wrinkle.

III. IMPACT OF He ION IRRADIATION ON THE THERMAL CONDUCTANCE

We continue to link the He-ion-induced changes in the superconducting thin film and the substrate to their thermal coupling, before showing in the subsequent section that this contributes substantially to the irradiation-induced performance enhancement of SNSPDs. The detection efficiency in SNSPDs is influenced not only by thin-film properties such as critical temperature, sheet resistance, and electron diffusivity but also by the thermal properties of the thin film and the superconductor–substrate interface. This is highlighted by the improved detection efficiency that Xu *et al.* achieved after reducing the thermal conductance between the superconducting thin film and the substrate by underetching the SNSPD.[64] Simulations in this work showed that samples with lower thermal conductance exhibit a longer hotspot decay time, meaning that the heat loss from the hotspot to the substrate is suppressed, thereby increasing the fraction of the photon energy that contributes to hotspot formation. We expect that the effects of He ion irradiation, such as the formation of He bubbles and the modification of the crystallinity of the Si substrate, may similarly reduce the thermal conductance and play an important role in the observed increase in detection efficiency of SNSPDs following irradiation. Therefore, we continue by investigating the impact of He ion irradiation on the thermal conductance between the superconducting thin film and the substrate in the following.

The equation governing heat flow in a one-dimensional nanowire is

$$J^2\rho + \kappa\frac{\partial^2 T}{\partial x^2} - \frac{\sigma}{d}(T^4 - T_{\mathrm{sub}}^4) = C\frac{\partial T}{\partial t}, \tag{1}$$

accounting for the heat flow along the nanowire, Joule heating from the resistive barrier when the nanowire is in the normal

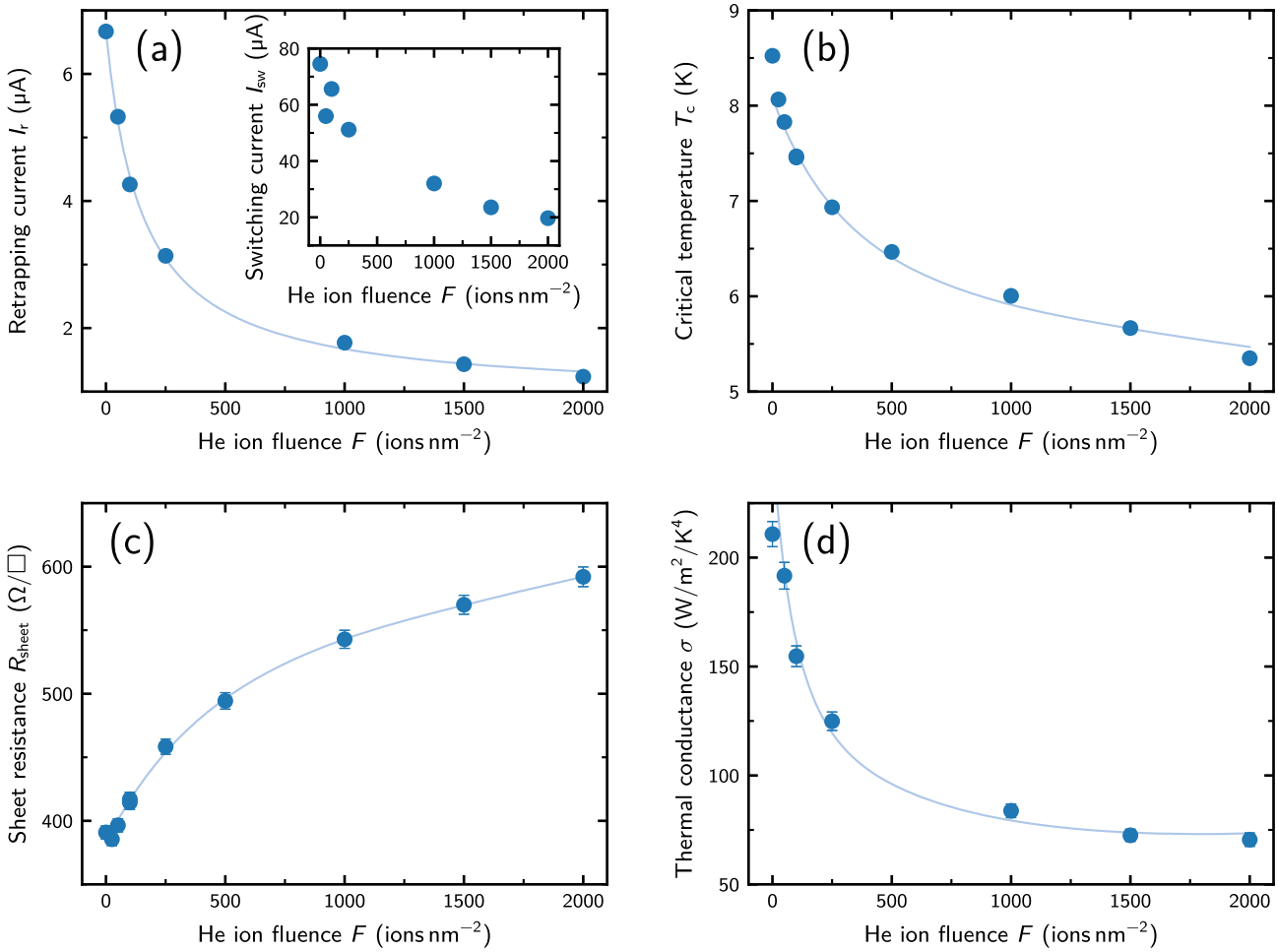

FIG. 4. Modification of basic transport properties and of the thermal conductance from the SNSPD to the substrate by He ion irradiation. (a) The retrapping current I_r with the switching current I_{sw} as inset, both measured at a temperature of 1 K. (b) The critical temperature T_c. (c) The sheet resistance R_{sheet}. (d) The thermal conductance between the superconducting thin film and the substrate σ. While the curves for I_r and σ are solely guides to the eye, the curves for T_c and R_{sheet} were fitted with the models described in the main text. Error bars are, in some cases, smaller than the symbols.

conducting state, and heat escaping from the superconducting thin film of thickness d to the substrate at a fixed substrate temperature T_{sub}.[64–69] Here, J is the current density, ρ is the normal-state resistivity, κ is the thermal conductivity of the superconducting nanowire, σ is the thermal conductance between the superconducting thin film and the substrate, and C is the specific heat per unit volume of NbTiN. According to the literature,[66,70] the thermal conductance σ can be obtained from the equation for the retrapping current density,

$$J_r = \sqrt{\frac{\sigma}{4d\rho}\left(T_c^4 - T_{sub}^4\right)}, \tag{2}$$

with the critical temperature T_c. To measure the retrapping current I_r, we pass a current above the switching current I_{sw} through the nanowire and then gradually reduce it until the normal conducting resistive domain within the nanowire can no longer sustain itself by Joule heating. This current, at which it switches back to the superconducting state, defines the retrapping current. We measured I_r for 25.8 μm long, 250 nm wide, and 8 nm thick nanowires at a temperature of 1 K, irradiated with He ion fluences ranging from 0 to 2000 ions nm^{-2}. As shown in Fig. 4(a), the largest decrease in I_r occurs at fluences smaller than 250 ions nm^{-2}, and it reduced from 6.7 to 1.2 μA comparing the unirradiated device to the device after irradiation with 2000 ions nm^{-2}. Moreover, in the inset of Fig. 4(a), we present the measured switching current of the same devices and observed the expected decrease with increasing He ion fluence that has already been reported in the literature.[34,35] In addition to the retrapping and the switching current, we measured the critical temperature and the sheet resistance of the irradiated films using cloverleaf structures fabricated on the same sample as the nanowire devices, following the van der Pauw method as described in previous work.[35,71,72] As shown in Figs. 4(b) and 4(c), the critical temperature decreases, while the sheet resistance increases with increasing He ion fluence. We fitted the sheet resistance using a model from our previous work[35] that accounts for defect formation in the NbTiN film and relate the critical temperature to the ion fluence via the sheet resistance by using the universal scaling law of Ivry *et al.*[73] Our sheet resistance model shows good agreement with the experimental data, while the derived critical temperature values exhibit slight deviations from measurements at both low and high He ion fluence. With these ingredients and the substrate temperature T_{sub} = 1 K, we calculate the thermal conductance σ via Eq. (2). As shown in Fig. 4(d), it decreased from initially 210 to 70 W m^{-2} K^{-4} after irradiation with 2000 ions nm^{-2}. Moreover, the data suggest a saturating thermal conductance for fluences above 1500 ions nm^{-2}. This can be explained by considering two paths contributing to the total thermal conductance: (1) a path where heat escapes normal to the wafer surface through the irradiated area, σ_{norm}, and (2) a path where heat flows in-plane, parallel to the wafer surface, $\sigma_{in\text{-}plane}$. Since the He bubbles form deep within the substrate and the He ions deposit most of their energy there, we expect that He ion irradiation primarily reduces σ_{norm} deep inside the substrate and underneath the irradiated area. At the same time, we expect $\sigma_{in\text{-}plane}$ in the NbTiN film and in the first nanometers underneath the film to be less affected by the irradiation. Above a sufficiently high He ion fluence, the in-plane thermal conductance starts to dominate and the total thermal conductance saturates at a value determined by the lateral dimensions of the irradiated area and the thickness of the thermally conducting channel. The thermal conductance of the unirradiated NbTiN films in this work is 210 W m^{-2} K^{-4}, which is comparable to but slightly below the lower bound of the range reported in the literature for the related material NbN (229–711 W m^{-2} K^{-4}).[64,66,69] To our knowledge, no thermal conductance values have been previously reported specifically for NbTiN films. While NbN and NbTiN share similar superconducting properties, variations in thermal conductance could be attributed to compositional and structural differences between these materials.

In summary, the thermal conductance between the superconducting thin film and the substrate decreases continuously with increasing He ion fluence, and after irradiation with 2000 ions nm^{-2}, it saturates at only 33% of the value for the unirradiated device. The reduced thermal conductance can have multiple origins such as (1) the He bubbles that form deep inside the substrate and act as a thermally insulating layer, (2) the irradiation-induced amorphization of the originally crystalline Si,[74,75] and (3) a modified superconductor–substrate interface due to the relaxation of internal stress in the NbTiN.

IV. ENHANCING DETECTION EFFICIENCY BY ENGINEERING THE THERMAL CONDUCTANCE

In the previous sections, we elaborated that the most prominent irradiation-induced changes of the NbTiN film and the underlying SiO_2/Si substrate are the wrinkling of the NbTiN film, the amorphization of the first few hundred nanometers of Si, and the formation of He bubbles in a region extending from approximately the SiO_2/Si interface (located at 150 nm depth) to about 340 nm depth. In addition to the fact that point defects are not visible in our TEM images of the NbTiN films, we also did not observe any changes in crystallinity or amorphization of the NbTiN film with increasing He ion fluence. Therefore, we conclude that in addition to the direct impact of irradiating the NbTiN film, a significant contribution to the enhanced sensitivity of SNSPDs following He ion irradiation[33–35] arises from a change in the thermal conductance between the superconducting thin film and the substrate.

To verify that changes in detector performance after irradiation cannot solely be explained by the direct irradiation effects on the NbTiN film, we compare three different irradiation schemes: (1) an unirradiated reference device, (2) a device fully irradiated with 2000 ions nm^{-2}, and (3) a device where we irradiated only the surrounding regions up to a distance of 150 nm from the edge of the superconducting wire with 2000 ions nm^{-2}. The He ion beam was focused to nanometer resolution, ensuring precise control of the irradiated regions with minimal beam spread at the sample surface. The focused He ion beam enters the substrate, where, through scattering and recoil events, the He ions successively transfer their energy to the substrate while spreading laterally as they move through it. Due to this lateral straggle, we expect the He ions to amorphize the Si and create He bubbles deep inside the substrate not only in the directly irradiated regions but also underneath the nanowire for the device where we irradiated only the regions next to the superconducting wire. This will modify the thermal conductance to the substrate while keeping the direct effects of He ions on the NbTiN wire limited. Appendix G contains a detailed discussion

about the simulated He ion distribution and energy deposition, and about the limitations of this particular irradiation scheme. We conclude that if a direct modification of the NbTiN wire by the He ion beam was the one and only cause for a change in detector properties, an irradiation of the surrounding area should have a very limited influence on them.

As shown in Figs. 5(a) and 5(b), our experiments with SNSPDs consisting of 250 nm wide and 8 nm thick nanowires at a temperature of 1 K demonstrate that both irradiated devices exhibit saturating detection efficiency at a wavelength of 780 nm, while the unirradiated device does not reach saturation. To further characterize these detectors, we define what we term the *photon-assisted critical current*, $I_{c,pa}$, as the minimum current at which the SNSPD shows non-zero resistance under constant illumination with photons of 780 nm wavelength. We note that the conventional critical current is defined as the current where a superconductor transitions from the superconducting to the normal conducting state in dark conditions. However, in the context of SNSPDs operated with shunt resistors, the critical current is typically defined as the current where the SNSPD transitions to a state where it shows, on average, a non-zero resistance in dark conditions—being either in a continuously normal conducting state or a state where the SNSPD shows relaxation oscillations.[76] While we could measure the photon-assisted critical current for all devices in this section, the critical current in dark conditions could not be determined for all devices since not all of them exhibited dark counts or relaxation oscillations with the 10.2 Ω shunt resistor and 1 s integration time used in these experiments. Nevertheless, the photon-assisted measurement ensures a consistent comparison across all devices, though we note that photon absorption can trigger the superconducting-to-normal transition at currents below the dark critical current. Using this definition, we observe that the photon-assisted critical current of the fully irradiated device is reduced to 22.4 μA, while the device where only the surrounding area was irradiated exhibits a similar value as the unirradiated device (59.0 and 60.1 μA, respectively). At the same time, we measured the switching current in these experiments without a shunt resistor (since a shunt resistor influences the nominal switching current[77]) and without illumination and observed its reduction not only for the fully irradiated device but also for the device where only the surrounding area was irradiated. Table I shows a comparison of these currents for the different devices before and after irradiation. The fact that the switching current is lower than the photon-assisted critical current for the devices with the full wire or the surrounding area irradiated might be explained by latching, since for switching current measurements no shunt resistor was connected. Surprisingly, the switching current for the unirradiated device is higher than its photon-assisted critical current. However, when comparing the two devices "surrounding irradiated" and "fully irradiated," a clear trend can be observed: despite the switching current for both devices being reduced after irradiation, the reduction is much less pronounced for the device with the surrounding area irradiated (42.5 μA compared to 19.7 μA, corresponding to reductions by 47% and 79%). This is even more apparent when comparing the photon-assisted critical current after and the switching current

TABLE I. Comparison of photon-assisted critical currents and switching currents (in μA) of the three devices discussed in Sec. IV. The unirradiated device was always measured as a reference device and, also in the rows "I_{sw} after irradiation" as well as "$I_{c,pa}$ after irradiation," it was never irradiated.

	Unirr.	Surr. irr.	Fully irr.
I_{sw} before irradiation	79.1	80.8	95.2
I_{sw} after irradiation	74.5	42.5	19.7
$I_{c,pa}$ after irradiation	60.1	59.0	22.4

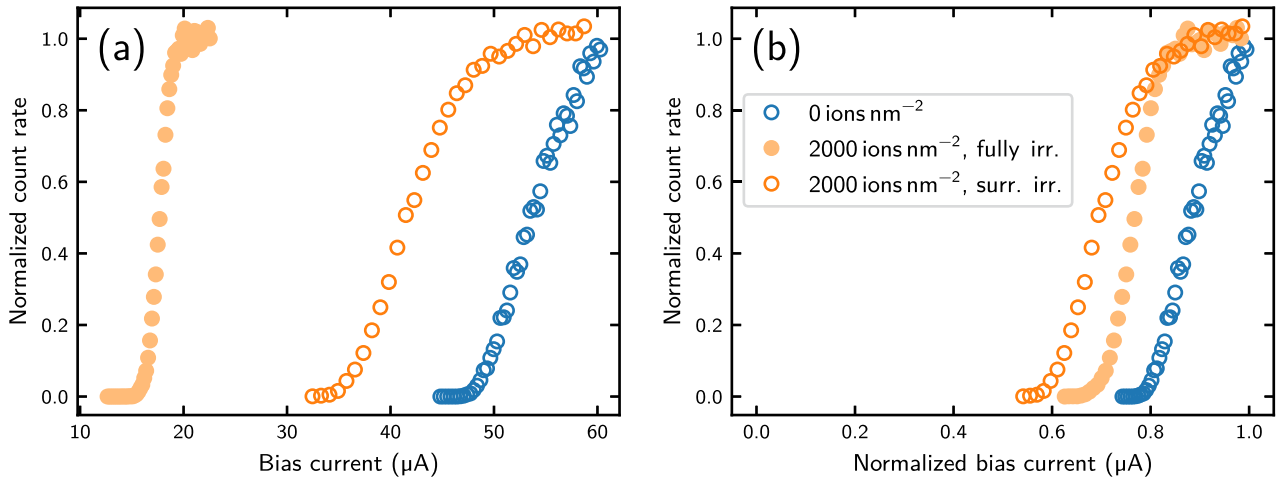

FIG. 5. Normalized count rate vs bias current for three differently irradiated SNSPDs (unirradiated, fully irradiated with 2000 ions nm^{-2}, and only the surrounding area irradiated with 2000 ions nm^{-2}). (a) The count rate is normalized to the fit asymptote after fitting an error function[78] and plotted against the absolute bias current. (b) The same data as in (a) but with the bias current normalized to the photon-assisted critical current of the SNSPD. The measurements were performed at a wavelength of 780 nm and a temperature of 1 K.

before irradiation (a reduction by 27% compared to 76%). The fact that the switching current of the device where only the surrounding area was irradiated is also reduced might be explained by He ions that reach the nanowire due to backscattering and recoil events as elaborated in Appendix G.

Examining the count rate curves in Fig. 5 in more detail, it is noteworthy that the relative saturation plateau width is of similar size (16.6%), and the absolute saturation plateau width is substantially larger for the wire with only the surrounding area irradiated compared to the fully irradiated wire (9.8 μA compared to 3.7 μA). This is particularly interesting since the wire itself was not irradiated and, moreover, the number of He atoms underneath the wire is on average only 3.9% of that underneath the fully irradiated wire (see Appendix G). We note that even if the photon-assisted critical current of the unirradiated device had been higher than, and not similar to, that of the surrounding irradiated device, the switching current and the photon-assisted critical current of the device for which the surrounding area was irradiated would still be substantially higher than those of the fully irradiated device, while their relative saturation plateau width is similar. These observations imply that irradiating only the surrounding area increases the sensitivity due to the reduced thermal conductance to the substrate, and simultaneously the sensitivity stays high since the photon-assisted critical current is barely reduced. In contrast, we typically observe a strong reduction of the critical current after full irradiation of SNSPDs.[35] This suggests that for devices where only the surrounding area is irradiated, higher He ion fluences might be explored in future work to potentially achieve even larger saturation plateau widths.

The most important conclusion of this experiment is that despite irradiating only the surrounding region of the nanowire, its sensitivity to single photons increased significantly. This would not be possible if a modification of the NbTiN via direct He ion irradiation was the only cause for a change in detector properties after irradiation. Thus, other mechanisms such as the irradiation-induced reduction of the thermal conductance from the detector to the substrate substantially contribute to the change in detector properties after irradiation.

V. CONCLUSION

Motivated by the significant improvement of SNSPD performance following He ion irradiation,[33–35] we investigated the irradiation-induced changes of the superconducting NbTiN films and the underlying SiO_2/Si substrates. Through combined TEM and AFM analysis, we found that irradiating the NbTiN/SiO_2/Si stack with 30 kV He ions transforms the crystalline Si into an amorphous structure, with He bubbles forming between the SiO_2/Si interface (at 150 nm depth) and 340 nm depth, causing substrate swelling. At the same time, the NbTiN film remains polycrystalline with columnar crystalline domains and an oxygen-rich top layer. However, the originally flat NbTiN film exhibits increasing wrinkling with increasing He ion fluence since the stress in the as-sputtered NbTiN film can be released due to viscous flow of the SiO_2, which allows its plastic deformation during He ion irradiation.

Moreover, experiments revealed a decrease in the thermal conductance from the NbTiN to the substrate with increasing He ion fluence from initially 210 to 70 W m^{-2} K^{-4} after irradiation with 2000 ions nm^{-2}. Combined with the observations of the influence of He ion irradiation on film and substrate morphology, this suggests the following: in addition to the effects of direct He ion irradiation on the NbTiN film, a substantial contribution to the enhanced SNSPD performance originates from an irradiation-induced reduction of the thermal conductance. This reduction, caused by He bubbles, amorphization of crystalline Si, and a modified NbTiN–SiO_2 interface, leads to a prolonged lifetime of the normal-conducting domain, thereby increasing the detection probability. To verify this hypothesis, we irradiated the surrounding area of a straight nanowire up to a distance of 150 nm from the wire. Due to scattering, the He ions spread laterally when moving through the sample and result in a reduced thermal conductance also underneath the nanowire. Although we did not irradiate the nanowire directly, we observed a similar relative saturation plateau width (16.6%), a significantly larger absolute saturation plateau width (9.8 μA compared to 3.7 μA), and a higher photon-assisted critical current (59.0 μA compared to 22.4 μA) after irradiation of the surrounding area of the nanowire with 2000 ions nm^{-2}, compared to full irradiation with the same He ion fluence. This confirms that the reduced thermal conductance substantially contributes to the enhanced sensitivity following He ion irradiation. Moreover, irradiation of the area surrounding the nanowire provides a means to reduce the thermal conductance underneath the nanowire while maintaining a high photon-assisted critical current due to the limited interaction of He ions with the NbTiN film.

To further differentiate the effects of the He ions on the NbTiN film vs the substrate, it would be desirable to compare detectors fabricated on pre-irradiated substrate regions with those fabricated on unirradiated substrate regions and then irradiated. Moreover, since the He implantation depth—which also defines the thickness of the heat conducting channel—can be tuned via the acceleration voltage, investigating the influence of different acceleration voltages on both device and substrate properties could provide valuable insights for optimizing detector performance.

ACKNOWLEDGMENTS

The authors highly appreciate FIB sample preparation by Dr. Steffen Schmidt. In preparing this manuscript, we utilized generative AI assistants including Claude.ai, ChatGPT, and Perplexity.ai, which provided support with manuscript revision, development of analysis scripts, and literature research under human supervision and verification. We gratefully acknowledge support from the German Federal Ministry of Education and Research (BMBF) via the funding program "Photonics Research Germany" [projects MOQUA (Grant No. 13N14846) and MARQUAND (Grant No. BN106022)] and the funding program "Quantum technologies – from basic research to market" [projects PhotonQ (Grant No. 13N15760), SPINNING (Grant No. 13N16214), QPIS (Grant No. 16K1SQ033), QPIC-1 (Grant No. 13N15855) and SEQT (Grant No. 13N15982)], as well as from the German Research Foundation (DFG) under Germany's Excellence Strategy EXC-2111 (Grant No. 390814868) with the projects PQET (Grant No. INST 95/1654-1) and MQCL (Grant No. INST 95/1720-1). This research is part of the "Munich Quantum Valley," which is supported by the Bavarian state government with funds from the "Hightech Agenda Bayern Plus."

AUTHOR DECLARATIONS

Conflict of Interest

The authors have no conflicts to disclose.

Author Contributions

S.S. and F.W. contributed equally to this work.

Stefan Strohauer: Conceptualization (lead); Data curation (equal); Formal analysis (equal); Investigation (equal); Methodology (equal); Project administration (lead); Resources (equal); Software (lead); Supervision (equal); Validation (equal); Visualization (lead); Writing – original draft (lead); Writing – review & editing (equal). **Fabian Wietschorke**: Conceptualization (equal); Data curation (equal); Formal analysis (equal); Investigation (equal); Methodology (equal); Project administration (supporting); Resources (equal); Software (supporting); Validation (equal); Visualization (equal); Writing – original draft (equal); Writing – review & editing (equal). **Markus Döblinger**: Conceptualization (equal); Formal analysis (equal); Investigation (equal); Methodology (equal); Resources (equal); Validation (equal); Visualization (equal); Writing – original draft (equal); Writing – review & editing (equal). **Christian Schmid**: Writing – review & editing (equal). **Stefanie Grotowski**: Writing – review & editing (equal). **Lucio Zugliani**: Writing – review & editing (equal). **Björn Jonas**: Writing – review & editing (equal). **Kai Müller**: Conceptualization (supporting); Funding acquisition (equal); Supervision (equal); Writing – review & editing (equal). **Jonathan J. Finley**: Conceptualization (supporting); Funding acquisition (equal); Supervision (equal); Writing – review & editing (equal).

DATA AVAILABILITY

The data that support the findings of this study are openly available in Harvard Dataverse at http://doi.org/10.7910/DVN/QQ31HM.

APPENDIX A: FABRICATION AND CHARACTERIZATION OF NbTiN FILMS AND SNSPDs

To fabricate the superconducting NbTiN films and SNSPDs studied in this work, we deposited NbTiN films using DC reactive magnetron sputtering onto two Si substrates (5×5 μm^2) with a nominally 130 nm thick thermally grown SiO_2 layer. The superconductor thickness was controlled by measuring the sputtering rate and choosing the sputtering time correspondingly. On the sample that was later used for AFM and TEM measurements, we deposited a nominally 12 nm thick NbTiN layer. Subsequent TEM images revealed an actual thickness of (11.3 ± 0.5) nm. On the other sample, we deposited a nominally 8 nm thick NbTiN layer for fabricating SNSPDs in the form of straight nanowires of 250 nm width and 25.8 μm length to study the influence of He ion irradiation on the thermal conductance between the superconducting thin film and the substrate and the associated change in detection efficiency. On the nanowire sample, we patterned the NbTiN film with electron beam lithography and reactive ion etching, followed by contact pad fabrication using optical lithography and gold evaporation. The process for contact pad fabrication was also used to fabricate gold marker structures on the sample for AFM and TEM measurements.

After characterization of the unirradiated devices, we used a He ion microscope (Zeiss Orion Nanofab) with an acceleration voltage of 30 kV for irradiation with He ions. On the nanowire sample, we fabricated three types of devices: (1) unirradiated nanowires, (2) fully irradiated nanowires, and (3) nanowires for which only the surrounding area was irradiated, leaving the nanowire and a 150 nm wide stripe next to the nanowire unirradiated. On the AFM/TEM sample, we used the He ion microscope to irradiate 4×4 and 15×15 μm^2 squares of the NbTiN film. Subsequently, we measured those irradiated areas with an AFM (Bruker Dimension Icon) using the ScanAsyst mode and an OTESPA tip.

Cross-sectional TEM lamellae were prepared from three regions: an unirradiated square and squares irradiated with 500 and 2000 ions nm^{-2}. Using a focused ion beam microscope (FEI Helios G3 UC), we thinned these sections to ~10–35 nm in the vicinity of the NbTiN film. The lamellae were characterized using a probe-corrected transmission electron microscope (FEI Titan Themis) operated at 300 kV, employing (scanning) transmission electron microscopy [(S)TEM], high-angle annular dark-field imaging (HAADF), and energy-dispersive x-ray spectroscopy (EDX). All images presented in Fig. 1 were acquired using HAADF-STEM.

APPENDIX B: PARTIAL RETENTION OF Si CRYSTALLINITY NEAR THE SiO_2/Si INTERFACE AFTER IRRADIATION WITH 500 ions nm^{-2}

After irradiation with 500 ions nm^{-2}, the Si substrate exhibits a distinct transition region near the SiO_2 interface where crystalline and amorphous phases coexist, as shown in Fig. 6. This partial preservation of crystallinity stands in contrast to the complete amorphization observed at 2000 ions nm^{-2}, indicating that the transformation process depends strongly on the He ion fluence. The high-resolution inset in Fig. 6 reveals clear lattice fringes in the

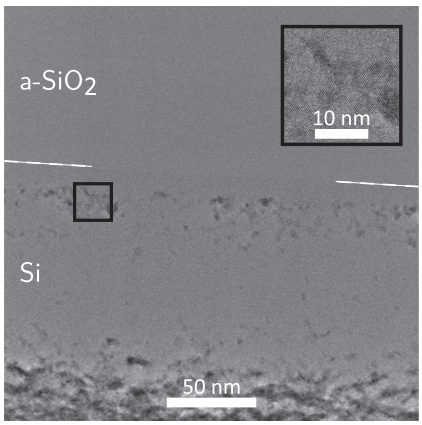

FIG. 6. TEM image of the interfacial region between amorphous SiO_2 and Si in the NbTiN/SiO_2/Si stack after irradiation with 500 ions nm^{-2}. The interface is marked by a dashed white line. Light gray regions indicate amorphous material and darker areas reveal crystalline silicon. The inset (3× magnification) shows a partially crystalline region where lattice fringes are clearly visible, demonstrating the local crystalline order.

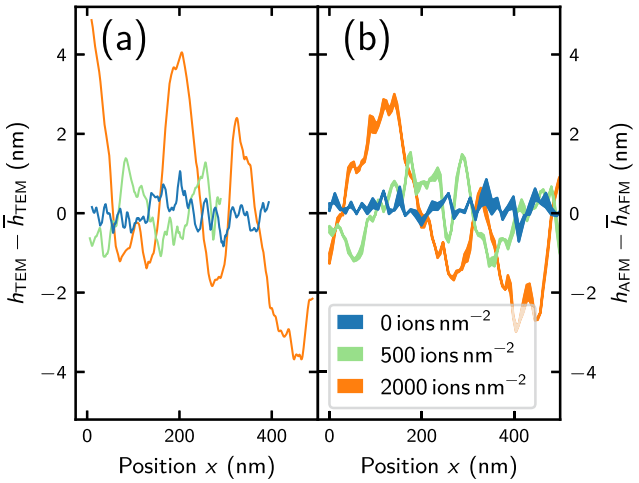

FIG. 7. Local deviation from the surface height average, $h - \bar{h}$, as determined by (a) TEM and (b) AFM measurements of the unirradiated NbTiN film and after irradiation with 500 and 2000 ions nm^{-2}. The local width of the lines in (b) is defined by the local height range bounded by the AFM line profiles obtained from the two averaging widths (12 and 35 nm).

preserved crystalline domains, providing direct evidence of residual crystalline order in these regions.

APPENDIX C: NbTiN FILM WRINKLING AND SURFACE ROUGHNESS

The TEM measurements presented in Sec. II reveal that the NbTiN film maintains its thickness after irradiation while exhibiting increasing wrinkling, characterized by synchronized undulations of its top and bottom surfaces. To quantify this wrinkling and compare it with AFM measurements, Fig. 7(a) shows the local deviation from the mean surface height of the NbTiN layer as determined from the TEM images. The analysis reveals that the local surface height varies within intervals of 1.8, 2.5, and 8 nm around the mean surface height for the film before He ion irradiation and after exposure to 500 and 2000 ions nm^{-2}, respectively. To compare this wrinkling with the AFM-measured surface roughness presented in Sec. II, Fig. 7(b) shows line profiles from three AFM images for the same He ion fluences. Each height value along these profiles is the local average across a strip oriented perpendicular to the profile direction, using widths of 12 and 35 nm to match the thickness range of the TEM lamellae. The local width of the lines in Fig. 7(b) is defined by the local height range, bounded by the profiles obtained from the two averaging widths, and indicates that both yield similar results. The AFM line profiles exhibit surface height variations within intervals of 1.6, 3, and 6 nm around the mean surface height for the unirradiated film and after exposure to 500 and 2000 ions nm^{-2}, respectively. These values, as well as their characteristic length scales of variation, closely match those derived from the TEM images, demonstrating quantitative agreement between both measurement techniques. Based on these results, we conclude that the AFM line profiles and rms roughness presented here and in Sec. II not only show continuously increasing surface height variations with increasing He ion fluence but can also be used to estimate the wrinkling of the NbTiN film observed in TEM images. To conclude, the increase in the AFM-measured surface roughness with increasing He ion fluence, combined with the correlation between surface roughness and wrinkling, indicates that the NbTiN film undergoes wrinkling rather than developing surface roughness with increasing He ion fluence.

APPENDIX D: ENERGY-DISPERSIVE X-RAY SPECTROSCOPY

For compositional analysis of the NbTiN film and the NbTiN/SiO_2/Si stack, we performed energy-dispersive x-ray

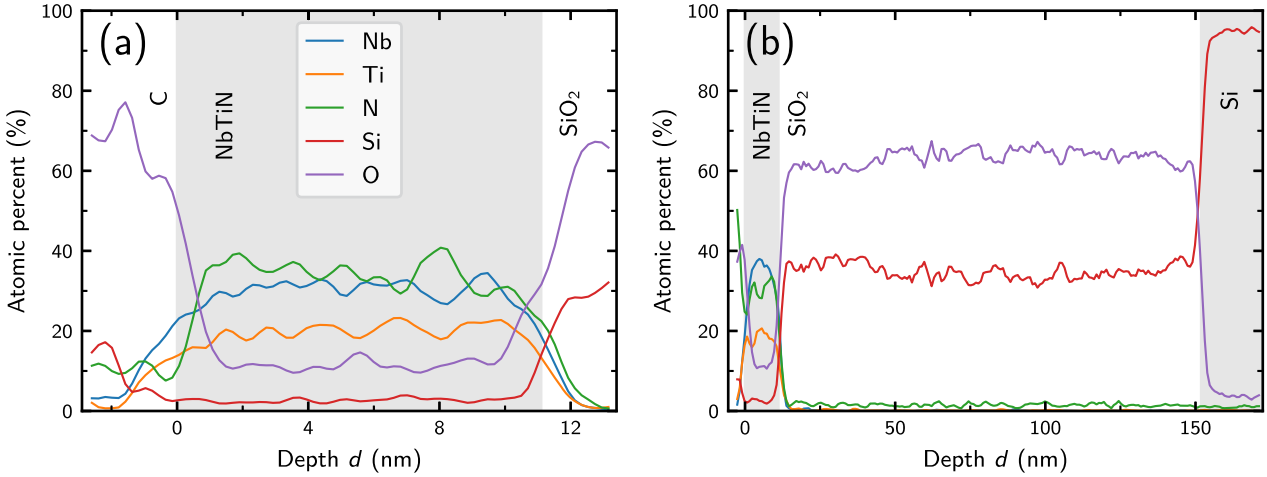

FIG. 8. Energy-dispersive x-ray spectroscopy (EDX) line profiles extracted from STEM-EDX maps of the unirradiated NbTiN/SiO_2/Si stack. The profiles were taken perpendicular to the interfaces, with integration performed parallel to them. (a) High-resolution scan across the NbTiN film (20 nm integration width), showing the SiO_2 support (right), the NbTiN film with its oxygen-rich surface layer (center), and a protective carbon layer required for sample preparation (left). Carbon was excluded from the elemental quantification to prevent distortion from its residual presence throughout the sample. (b) Wide-area scan across the complete NbTiN/SiO_2/Si stack (58 nm integration width).

spectroscopy (EDX) using scanning transmission electron microscopy (STEM). From these EDX maps, we extracted integrated compositional profiles perpendicular to the interfaces, as shown in Fig. 8.

APPENDIX E: INFLUENCE OF THE ANNEALING TEMPERATURE ON THE SURFACE ROUGHNESS

In this section, we investigate how stress in the originally flat NbTiN film can relax and deform the NbTiN film by heating the sample to temperatures above 960 °C, where viscous flow of thermally grown SiO_2 starts.[63] To this aim, we mounted a sample with the stack NbTiN/SiO_2/Si in a chamber that was purged with nitrogen and evacuated to a pressure range of 10^{-7}–10^{-8} mbar before ramping up the temperature and holding the target temperature for 30 min. Figure 9 shows the AFM images and line profiles across the surface before and after heating to 800 and 1050 °C. We note that the sample used in this heating experiment exhibited unusual surface features (potentially originating from a contaminated surface prior to the sputtering process) that grew in size when heated to 1050 °C. Therefore, we placed the line profiles in regions without those grains. While the line profiles before and after heating the sample to 800° show a similar rms roughness of 0.27 and 0.24 nm, it increases to 2.25 nm after heating to 1050 °C. This indicates that stress in the NbTiN film is already present after sputtering and that it relaxes when enabling viscous flow of the underlying substrate.

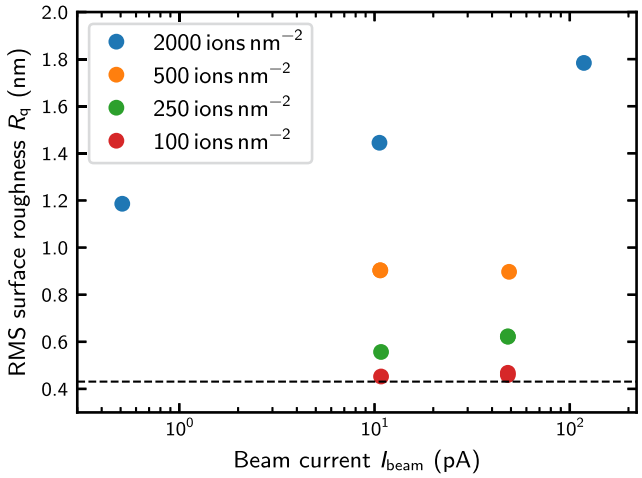

FIG. 10. rms surface roughness vs beam current used for irradiation with He ion fluences ranging from 100 to 2000 ions nm^{-2}. The black dashed line indicates the rms surface roughness before irradiation.

APPENDIX F: INFLUENCE OF THE BEAM CURRENT ON THE SURFACE ROUGHNESS

To investigate the influence of the beam current on the roughness/wrinkling of the NbTiN film, we irradiated the stack NbTiN/SiO_2/Si with beam currents ranging from 0.5 to 118 pA. Figure 10 shows the rms surface roughness after irradiation as

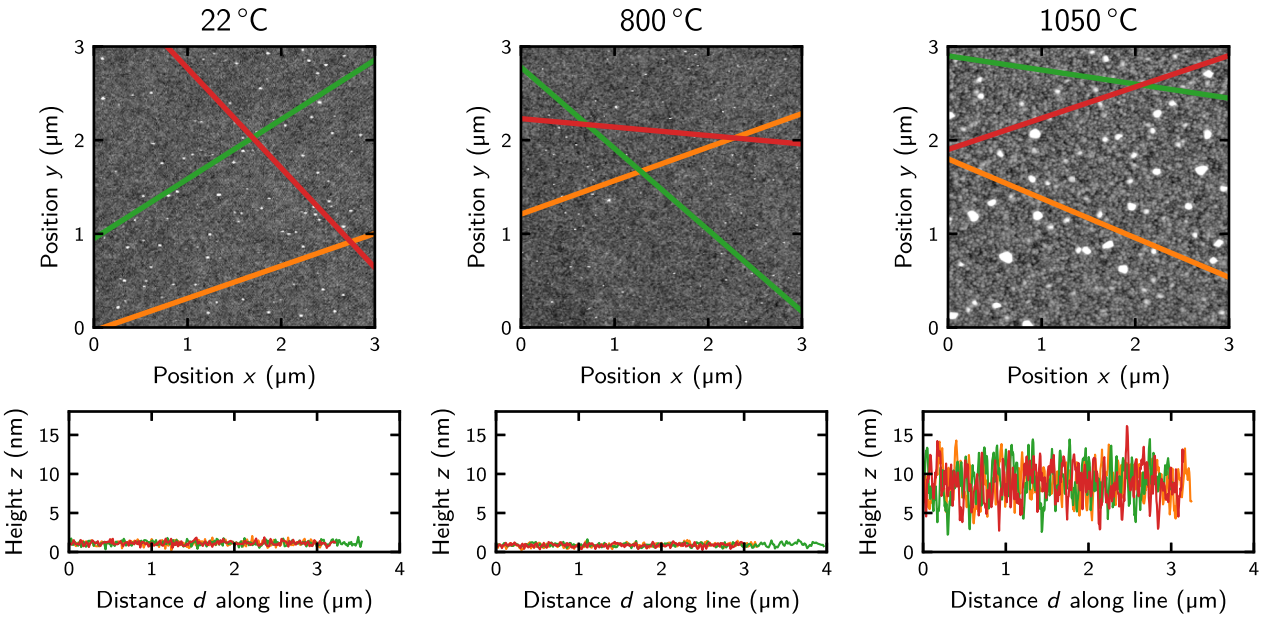

FIG. 9. AFM measurements and corresponding line profiles of the stack NbTiN/SiO_2/Si after exposing it to three different temperatures. The as-sputtered film and the film after heating it to 800 °C exhibit a similar rms roughness of 0.27 and 0.24 nm, respectively. This increases to 2.25 nm after heating the sample to 1050 °C.

measured with an AFM. The roughness increases from 0.43 nm before irradiation to 1.19 and 1.78 nm for the lowest and highest beam current, respectively. We explain this difference by increased viscous flow of the SiO_2 at higher beam currents, allowing more relaxation of the stress that built up in the NbTiN during the sputtering process. However, even for the smallest beam currents, the roughness increased by a factor of three after irradiation with 2000 ions nm^{-2} compared to the unirradiated film.

APPENDIX G: He ION DISTRIBUTION FOR DISTANT IRRADIATION

In this section, we estimate the relative amount of implanted He ions and deposited energy in and underneath a 250 nm wide NbTiN wire when irradiating only the surrounding area up to a distance of 150 nm from the wire and compare it to a fully irradiated wire. The average lateral spread of He ions when irradiating a single spot can be calculated by projecting the simulated three-dimensional stopping positions of He ions onto a line parallel to the surface, resulting in a Gaussian distribution with a FWHM of 266 nm. When irradiating only the regions next to the superconducting wire, this lateral spread will result in a significant fraction of He ions underneath the nanowire. The relative fraction of implanted He ions f_{rel} along a line perpendicular to the nanowire can be calculated by taking the convolution of the Gaussian distribution of He ions with the one-dimensional profile of irradiation along this line:

$$f_{\mathrm{rel}}(x) = \int_{-\infty}^{\infty} \frac{1}{\sqrt{2\pi\sigma^2}} e^{-\frac{(s-x)^2}{2\sigma^2}} \cdot \Theta\left(|s| - \frac{w_{\mathrm{unirr}}}{2}\right) \mathrm{d}s\,, \qquad \text{(G1)}$$

with the standard deviation σ of the Gaussian distribution, the width w_{unirr} of the unirradiated area, and the Heaviside step function Θ. The resulting He ion distribution is shown as an orange line in Fig. 11(a), with the minimum and maximum amounts of He ions underneath the nanowire being 1.5% and 9.3%, and an average amount of 3.9% of that in the fully irradiated area.

As shown in Fig. 2(b), the FWHM of the He ion stopping positions within the NbTiN layer is 400 nm due to recoil events and scattering. Following the same procedure as above, but projecting only the stopping positions of He ions that end up in the 12 nm thick NbTiN film onto a line perpendicular to the nanowire, we calculate the convolution of the resulting Gaussian distribution with the one-dimensional irradiation profile and obtain the relative fraction of He ions implanted in the nanowire, as presented as the green line in Fig. 11(a). Since the FWHM of the implanted He distribution in the NbTiN layer is higher than that when considering the stopping positions of all He ions, also the minimum and maximum relative fractions, 10.9% and 20.1%, and the average fraction of 14.0% are higher. This indicates that the number of He ions that stop within the NbTiN wire is of the same order of magnitude when comparing full irradiation with irradiation up to a distance of 150 nm from the wire. This leads to the question of how the effects of direct irradiation differ from irradiation up to a distance of 150 nm from the wire. According to the Bragg peak, the He ions deposit most energy per nm shortly before they stop, as can be seen in Fig. 11(b). However, the energy loss per nm when entering the sample is still half of that at the maximum at a 270 nm sample depth. Moreover, at the spots where the focused He ion beam hits the sample, all He ions deposit a fraction of their kinetic energy in the NbTiN film. Taking into account that only the fraction 10^{-4} of all ions end up in each nm of the NbTiN film, we conclude that the total energy deposited in the NbTiN wire when irradiating up to a distance of 150 nm from the wire is approximately four orders of magnitude smaller than when irradiating the whole device. We note, however, that the small

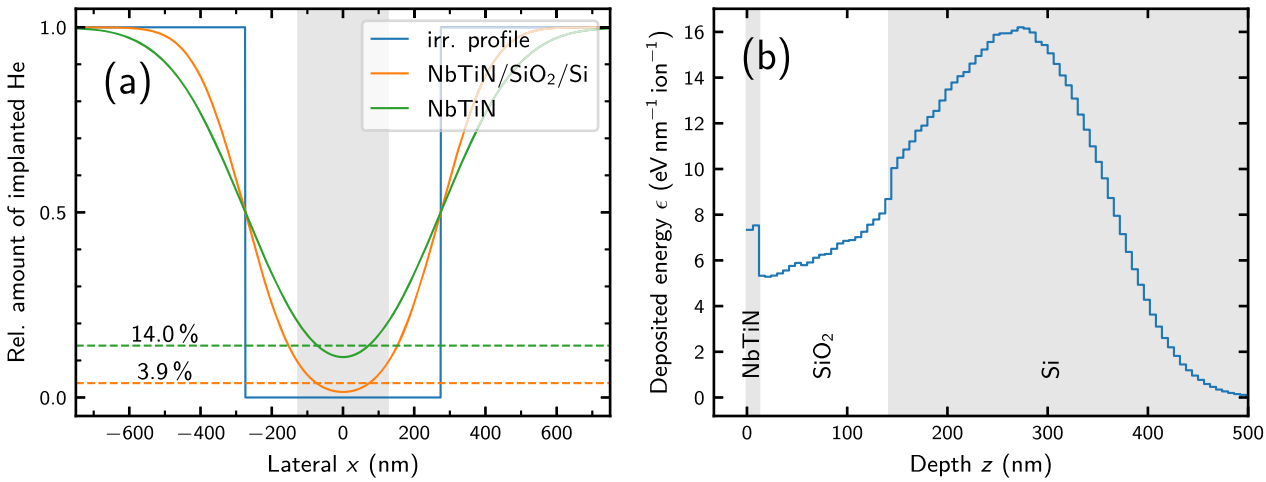

FIG. 11. Simulated He ion and energy distribution after irradiation of the sample stack NbTiN/SiO_2/Si in the surrounding area of the wire up to a distance of 150 nm from the wire. (a) Normalized implanted He ion distribution. The irradiation profile is shown as a blue line (1 in the regions where the He ion beam hits the surface), while the width of the nanowire is indicated by the gray shaded area. The orange line is the distribution of He ions integrated along the full depth of the sample (over the whole stack NbTiN/SiO_2/Si), while the green line is the distribution when integrating only over the NbTiN layer. Both distributions are normalized to the amount of implanted He for full irradiation. The corresponding average amount of implanted He underneath the wire is indicated by the horizontal dashed lines. (b) Deposited energy per ion and per nm sample depth. The material stack NbTiN/SiO_2/Si is indicated by the differently shaded areas.

fraction 10^{-4} of the He ions that are implanted in the NbTiN wire per nm is similar when comparing fully irradiated devices with those irradiated up to a distance of 150 nm from the wire. At the same time, the total amount of He ions implanted in the SiO_2/Si substrate underneath the nanowire is still 3.9% of that in the fully irradiated area, leading to substantial He bubble formation and a reduced superconductor-to-substrate thermal conductance underneath the nanowire.

Thus, when keeping the wire unirradiated and irradiating only its surroundings up to a distance of 150 nm from the wire, the NbTiN should be barely directly affected by the He ion beam (only by the small fraction of deflected or recoiled atoms/ions), while the reduced thermal conductance due to the amorphization of Si and the formation of He bubbles in the substrate extends under the nanowire.

We note that in addition to the amorphization of Si and the formation of He bubbles underneath the wire, we cannot completely exclude that the following two points also have some influence on device performance: (1) The curved surface due to the different surface elevation in the center vs the edges of the nanowire, which originates from smaller He bubbles underneath the center of the wire compared to the edges. (2) A potential residual plastic flow of the SiO_2 near the NbTiN interface due to the small amount of energy deposited in this region from scattered/recoiled He ions. However, since the fraction of energy is only on the order of 10^{-4} compared to the fully irradiated regions, we expect this effect to be negligible. To fully isolate the change in device properties due to the modified superconductor-to-substrate thermal conductance after irradiation, future studies comparing the performance of devices fabricated on pre-irradiated substrate regions to similar devices fabricated on unirradiated regions of the same substrate would be useful.

REFERENCES

[1] G. N. Gol'tsman, O. Okunev, G. Chulkova, A. Lipatov, A. Semenov, K. Smirnov, B. Voronov, A. Dzardanov, C. Williams, and R. Sobolewski, "Picosecond superconducting single-photon optical detector," Appl. Phys. Lett. **79**, 705–707 (2001).

[2] H. Takesue, S. W. Nam, Q. Zhang, R. H. Hadfield, T. Honjo, K. Tamaki, and Y. Yamamoto, "Quantum key distribution over a 40-dB channel loss using superconducting single-photon detectors," Nat. Photonics **1**, 343–348 (2007).

[3] J.-P. Chen, C. Zhang, Y. Liu, C. Jiang, D.-F. Zhao, W.-J. Zhang, F.-X. Chen, H. Li, L.-X. You, Z. Wang, Y. Chen, X.-B. Wang, Q. Zhang, and J.-W. Pan, "Quantum key distribution over 658 km fiber with distributed vibration sensing," Phys. Rev. Lett. **128**, 180502 (2022).

[4] Y. Liu, W.-J. Zhang, C. Jiang, J.-P. Chen, C. Zhang, W.-X. Pan, D. Ma, H. Dong, J.-M. Xiong, C.-J. Zhang, H. Li, R.-C. Wang, J. Wu, T.-Y. Chen, L. You, X.-B. Wang, Q. Zhang, and J.-W. Pan, "Experimental twin-field quantum key distribution over 1000 km fiber distance," Phys. Rev. Lett. **130**, 210801 (2023).

[5] F. Bussières, C. Clausen, A. Tiranov, B. Korzh, V. B. Verma, S. W. Nam, F. Marsili, A. Ferrier, P. Goldner, H. Herrmann, C. Silberhorn, W. Sohler, M. Afzelius, and N. Gisin, "Quantum teleportation from a telecom-wavelength photon to a solid-state quantum memory," Nat. Photonics **8**, 775–778 (2014).

[6] H. Takesue, S. D. Dyer, M. J. Stevens, V. Verma, R. P. Mirin, and S. W. Nam, "Quantum teleportation over 100 km of fiber using highly efficient superconducting nanowire single-photon detectors," Optica **2**, 832 (2015).

[7] H. Shibata, T. Honjo, and K. Shimizu, "Quantum key distribution over a 72 dB channel loss using ultralow dark count superconducting single-photon detectors," Opt. Lett. **39**, 5078 (2014).

[8] R. Valivarthi, M. G. Puigibert, Q. Zhou, G. H. Aguilar, V. B. Verma, F. Marsili, M. D. Shaw, S. W. Nam, D. Oblak, and W. Tittel, "Quantum teleportation across a metropolitan fibre network," Nat. Photonics **10**, 676–680 (2016).

[9] C. M. Natarajan, M. G. Tanner, and R. H. Hadfield, "Superconducting nanowire single-photon detectors: Physics and applications," Supercond. Sci. Technol. **25**, 063001 (2012).

[10] M. E. Grein, A. J. Kerman, E. A. Dauler, M. M. Willis, B. Romkey, R. J. Molnar, B. S. Robinson, D. V. Murphy, and D. M. Boroson, "An optical receiver for the Lunar Laser Communication Demonstration based on photon-counting superconducting nanowires," Proc. SPIE **9492**, 949208 (2015).

[11] A. Biswas, M. Srinivasan, R. Rogalin, S. Piazzolla, J. Liu, B. Schratz, A. Wong, E. Alerstam, M. Wright, W. T. Roberts, J. Kovalik, G. Ortiz, A. Na-Nakornpanom, M. Shaw, C. Okino, K. Andrews, M. Peng, D. Orozco, and W. Klipstein, "Status of NASA's deep space optical communication technology demonstration," in *2017 IEEE International Conference on Space Optical Systems and Applications (ICSOS)* (IEEE, Naha, 2017), pp. 23–27.

[12] E. E. Wollman, V. B. Verma, A. B. Walter, J. Chiles, B. Korzh, J. P. Allmaras, Y. Zhai, A. E. Lita, A. N. McCaughan, E. Schmidt, S. Frasca, R. P. Mirin, S. W. Nam, and M. D. Shaw, "Recent advances in superconducting nanowire single-photon detector technology for exoplanet transit spectroscopy in the mid-infrared," J. Astron. Telesc., Instrum. Syst. **7**, 011004 (2021).

[13] F. Xia, M. Gevers, A. Fognini, A. T. Mok, B. Li, N. Akbari, I. E. Zadeh, J. Qin-Dregely, and C. Xu, "Short-wave infrared confocal fluorescence imaging of deep mouse brain with a superconducting nanowire single-photon detector," ACS Photonics **8**, 2800–2810 (2021).

[14] F. Wang, F. Ren, Z. Ma, L. Qu, R. Gourgues, C. Xu, A. Baghdasaryan, J. Li, I. E. Zadeh, J. W. N. Los, A. Fognini, J. Qin-Dregely, and H. Dai, "In vivo non-invasive confocal fluorescence imaging beyond 1,700 nm using superconducting nanowire single-photon detectors," Nat. Nanotechnol. **17**, 653–660 (2022).

[15] A. Tamimi, M. Caldarola, S. Hambura, J. C. Boffi, N. Noordzij, J. W. N. Los, A. Guardiani, H. Kooiman, L. Wang, C. Kieser, F. Braun, M. A. U. Castaneda, A. Fognini, and R. Prevedel, "Deep mouse brain two-photon near-infrared fluorescence imaging using a superconducting nanowire single-photon detector array," ACS Photonics **11**, 3960–3971 (2024).

[16] N. Ozana, A. I. Zavriyev, D. Mazumder, M. Robinson, K. Kaya, M. Blackwell, S. A. Carp, and M. A. Franceschini, "Superconducting nanowire single-photon sensing of cerebral blood flow," Neurophotonics **8**, 035006 (2021).

[17] C.-S. Poon, D. S. Langri, B. Rinehart, T. M. Rambo, A. J. Miller, B. Foreman, and U. Sunar, "First-in-clinical application of a time-gated diffuse correlation spectroscopy system at 1064 nm using superconducting nanowire single photon detectors in a neuro intensive care unit," Biomed. Opt. Express **13**, 1344 (2022).

[18] V. Parfentyeva, L. Colombo, P. Lanka, M. Pagliazzi, A. Brodu, N. Noordzij, M. Kolarczik, A. Dalla Mora, R. Re, D. Contini, A. Torricelli, T. Durduran, and A. Pifferi, "Fast time-domain diffuse correlation spectroscopy with superconducting nanowire single-photon detector: System validation and in vivo results," Sci. Rep. **13**, 11982 (2023).

[19] D. V. Reddy, R. R. Nerem, S. W. Nam, R. P. Mirin, and V. B. Verma, "Superconducting nanowire single-photon detectors with 98% system detection efficiency at 1550 nm," Optica **7**, 1649 (2020).

[20] J. Chang, J. W. N. Los, J. O. Tenorio-Pearl, N. Noordzij, R. Gourgues, A. Guardiani, J. R. Zichi, S. F. Pereira, H. P. Urbach, V. Zwiller, S. N. Dorenbos, and I. Esmaeil Zadeh, "Detecting telecom single photons with (99.5−2.07+0.5)% system detection efficiency and high time resolution," APL Photonics **6**, 036114 (2021).

[21] H. Shibata, K. Shimizu, H. Takesue, and Y. Tokura, "Ultimate low system dark-count rate for superconducting nanowire single-photon detector," Opt. Lett. **40**, 3428 (2015).

[22] B. Korzh, Q. Y. Zhao, J. P. Allmaras, S. Frasca, T. M. Autry, E. A. Bersin, A. D. Beyer, R. M. Briggs, B. Bumble, M. Colangelo, G. M. Crouch, A. E. Dane, T. Gerrits, A. E. Lita, F. Marsili, G. Moody, C. Peña, E. Ramirez, J. D. Rezac, N. Sinclair, M. J. Stevens, A. E. Velasco, V. B. Verma, E. E. Wollman, S. Xie, D. Zhu, P. D. Hale, M. Spiropulu, K. L. Silverman, R. P. Mirin, S. W. Nam, A. G. Kozorezov, M. D. Shaw, and K. K. Berggren, "Demonstration of sub-3 ps temporal resolution with a superconducting nanowire single-photon detector," Nat. Photonics **14**, 250–255 (2020).

[23]S. Cherednichenko, N. Acharya, E. Novoselov, and V. Drakinskiy, "Low kinetic inductance superconducting MgB_2 nanowires with a 130 ps relaxation time for single-photon detection applications," Supercond. Sci. Technol. **34**, 044001 (2021).
[24]S. Slussarenko and G. J. Pryde, "Photonic quantum information processing: A concise review," Appl. Phys. Rev. **6**, 041303 (2019).
[25]S. Chen, D. Liu, W. Zhang, L. You, Y. He, W. Zhang, X. Yang, G. Wu, M. Ren, H. Zeng, Z. Wang, X. Xie, and M. Jiang, "Time-of-flight laser ranging and imaging at 1550 nm using low-jitter superconducting nanowire single-photon detection system," Appl. Opt. **52**, 3241 (2013).
[26]Y. Guan, H. Li, L. Xue, R. Yin, L. Zhang, H. Wang, G. Zhu, L. Kang, J. Chen, and P. Wu, "Lidar with superconducting nanowire single-photon detectors: Recent advances and developments," Opt. Lasers Eng. **156**, 107102 (2022).
[27]B. Kaifler, C. Geach, H. C. Büdenbender, A. Mezger, and M. Rapp, "Measurements of metastable helium in Earth's atmosphere by resonance lidar," Nat. Commun. **13**, 6042 (2022).
[28]C. Peña, C. Wang, S. Xie, A. Bornheim, M. Barría, C. S. Martín, V. Vega, A. Apresyan, E. Knehr, B. Korzh, J. Luskin, L. Narváez, S. Patel, M. Shaw, and M. Spiropulu, "High energy particle detection with large area superconducting microwire array," J. Instrum. **20**, P03001 (2025).
[29]T. Polakovic, W. Armstrong, G. Karapetrov, Z. E. Meziani, and V. Novosad, "Unconventional applications of superconducting nanowire single photon detectors," Nanomaterials **10**, 1198 (2020).
[30]M. Shigefuji, A. Osada, M. Yabuno, S. Miki, H. Terai, and A. Noguchi, "Efficient low-energy single-electron detection using a large-area superconducting microstrip," arXiv:2301.11212 [cond-mat, physics:physics, physics:quant-ph] (2023).
[31]Y. Hochberg, I. Charaev, S.-W. Nam, V. Verma, M. Colangelo, and K. K. Berggren, "Detecting sub-GeV dark matter with superconducting nanowires," Phys. Rev. Lett. **123**, 151802 (2019).
[32]J. Chiles, I. Charaev, R. Lasenby, M. Baryakhtar, J. Huang, A. Roshko, G. Burton, M. Colangelo, K. Van Tilburg, A. Arvanitaki, S. W. Nam, and K. K. Berggren, "New constraints on dark photon dark matter with superconducting nanowire detectors in an optical haloscope," Phys. Rev. Lett. **128**, 231802 (2022).
[33]S. Strohauer, F. Wietschorke, C. Schmid, S. Grotowski, L. Zugliani, B. Jonas, K. Müller, and J. J. Finley, "Current crowding–free superconducting nanowire single-photon detectors," Sci. Adv. **11**, eadt0502 (2025).
[34]W. Zhang, Q. Jia, L. You, X. Ou, H. Huang, L. Zhang, H. Li, Z. Wang, and X. Xie, "Saturating intrinsic detection efficiency of superconducting nanowire single-photon detectors via defect engineering," Phys. Rev. Appl. **12**, 044040 (2019).
[35]S. Strohauer, F. Wietschorke, L. Zugliani, R. Flaschmann, C. Schmid, S. Grotowski, M. Müller, B. Jonas, M. Althammer, R. Gross, K. Müller, and J. J. Finley, "Site-selective enhancement of superconducting nanowire single-photon detectors via local helium ion irradiation," Adv. Quantum Technol. **6**, 2300139 (2023).
[36]I. Charaev, E. K. Batson, S. Cherednichenko, K. Reidy, V. Drakinskiy, Y. Yu, S. Lara-Avila, J. D. Thomsen, M. Colangelo, F. Incalza, K. Ilin, A. Schilling, and K. K. Berggren, "Single-photon detection using large-scale high-temperature MgB_2 sensors at 20 K," Nat. Commun. **15**, 3973 (2024).
[37]E. Batson, F. Incalza, M. Castellani, M. Colangelo, I. Charaev, A. Schilling, S. Cherednichenko, and K. K. Berggren, "Effects of helium ion exposure on the single-photon sensitivity of MgB_2 and NbN detectors," IEEE Trans. Appl. Supercond. **34**, 0600906 (2024).
[38]A. Ruhtinas and I. J. Maasilta, "Highly tunable NbTiN Josephson junctions fabricated with focused helium ion beam," arXiv:2303.17348 [cond-mat] (2023).
[39]G. D. Martinez, D. Buckley, I. Charaev, A. Dane, D. E. Dow, and K. K. Berggren, "Superconducting nanowire fabrication on niobium nitride using helium ion irradiation," arXiv:2003.02898 (2020).
[40]R. Flaschmann, L. Zugliani, C. Schmid, S. Spedicato, S. Strohauer, F. Wietschorke, F. Flassig, J. J. Finley, and K. Müller, "The dependence of timing jitter of superconducting nanowire single-photon detectors on the multi-layer sample design and slew rate," Nanoscale **15**, 1086–1091 (2023).
[41]V. Raineri, S. Coffa, E. Szilágyi, J. Gyulai, and E. Rimini, "He-vacancy interactions in Si and their influence on bubble formation and evolution," Phys. Rev. B **61**, 937–945 (2000).
[42]R. Livengood, S. Tan, Y. Greenzweig, J. Notte, and S. McVey, "Subsurface damage from helium ions as a function of dose, beam energy, and dose rate," J. Vac. Sci. Technol. B **27**, 3244 (2009).
[43]K. J. Abrams, J. A. Hinks, C. J. Pawley, G. Greaves, J. A. Van Den Berg, D. Eyidi, M. B. Ward, and S. E. Donnelly, "Helium irradiation effects in polycrystalline Si, silica, and single crystal Si," J. Appl. Phys. **111**, 083527 (2012).
[44]G. Hlawacek, V. Veligura, R. Van Gastel, and B. Poelsema, "Helium ion microscopy," J. Vac. Sci. Technol. B **32**, 020801 (2014).
[45]F. I. Allen, "A review of defect engineering, ion implantation, and nanofabrication using the helium ion microscope," Beilstein J. Nanotechnol. **12**, 633–664 (2021).
[46]J. F. Ziegler, M. D. Ziegler, and J. P. Biersack, "SRIM—The stopping and range of ions in matter (2010)," Nucl. Instrum. Methods Phys. Res., Sect. B **268**, 1818–1823 (2010).
[47]G.-i. Oya and Y. Onodera, "Transition temperatures and crystal structures of single-crystal and polycrystalline NbN_x films," J. Appl. Phys. **45**, 1389–1397 (1974).
[48]G. Brauer and J. Jander, "Die nitride des niobs," Z. Anorg. Allg. Chem. **270**, 160–178 (1952).
[49]T. Yamamoto, S. Kikkawa, M. Takahashi, Y. Miyamoto, and F. Kanamaru, "High pressure synthesis of B1-type solid solutions $Nb_{1-x}M_xN$ (M = Ga, Ti)," Physica C **185–189**, 2719–2720 (1991).
[50]J. S. Custer, M. O. Thompson, D. C. Jacobson, J. M. Poate, S. Roorda, W. C. Sinke, and F. Spaepen, "Density of amorphous Si," Appl. Phys. Lett. **64**, 437–439 (1994).
[51]H.-S. Yoon, C.-S. Kim, H.-T. Lee, and S.-H. Ahn, "Advanced scanning paths for focused ion beam milling," Vacuum **143**, 40–49 (2017).
[52]M. D. Bachmann, *Manipulating Anisotropic Transport and Superconductivity by Focused Ion Beam Microstructuring*, *Springer Theses* (Springer International Publishing, Cham, 2020).
[53]S. Kajita, N. Yoshida, R. Yoshihara, N. Ohno, and M. Yamagiwa, "TEM observation of the growth process of helium nanobubbles on tungsten: Nanostructure formation mechanism," J. Nucl. Mater. **418**, 152–158 (2011).
[54]E. Snoeks, A. Polman, and C. A. Volkert, "Densification, anisotropic deformation, and plastic flow of SiO_2 during MeV heavy ion irradiation," Appl. Phys. Lett. **65**, 2487–2489 (1994).
[55]C. A. Volkert, "Stress and plastic flow in silicon during amorphization by ion-bombardment," MRS Proc. **157**, 635 (1989).
[56]C. A. Volkert, "Density changes and viscous flow during structural relaxation of amorphous silicon," J. Appl. Phys. **74**, 7107–7113 (1993).
[57]C. A. Volkert, "Stress and plastic flow in silicon during amorphization by ion bombardment," J. Appl. Phys. **70**, 3521–3527 (1991).
[58]N. N. Iosad, B. D. Jackson, T. M. Klapwijk, S. N. Polyakov, P. N. Dmitirev, and J. R. Gao, "Optimization of RF- and DC-sputtered NbTiN films for integration with Nb-based SIS junctions," IEEE Trans. Appl. Supercond. **9**, 1716–1719 (1999).
[59]T. W. Cecil, R. M. Weikle, A. R. Kerr, and A. W. Lichtenberger, "Investigation of NbTiN thin films and AlN tunnel barriers with ellipsometry for superconducting device applications," IEEE Trans. Appl. Supercond. **17**, 3525–3528 (2007).
[60]H. Yamamori, H. Sasaki, and S. Kohjiro, "Preparation of overdamped NbTiN Josephson junctions with bilayered Ti–TiN barriers," J. Appl. Phys. **108**, 113904 (2010).
[61]W. Shan, Y. Sekimoto, and T. Noguchi, "Microwave loss of DC sputtered NbTiN microstrip lines," Jpn. J. Appl. Phys. **54**, 090303 (2015).
[62]A. Karimi, D. La Grange, N. Goebbels, and A. Santana, "Structural and mechanical properties of $Nb_{1-x}Ti_xN$ thin films deposited by rf magnetron sputtering," Thin Solid Films **607**, 14–24 (2016).
[63]E. P. EerNisse, "Viscous flow of thermal SiO_2," Appl. Phys. Lett. **30**, 290–293 (1977).
[64]T. Xu, H. Bao, Z. Qin, X. Jia, G. Zhu, D. Pan, X. Tu, L. Zhang, Q. Zhao, L. Kang, J. Chen, and P. Wu, "Enhancing SNSPDs detection efficiency via suspended SiO_2 membrane," Appl. Phys. Lett. **123**, 082602 (2023).
[65]J. K. W. Yang, A. J. Kerman, E. A. Dauler, V. Anant, K. M. Rosfjord, and K. K. Berggren, "Modeling the electrical and thermal response of superconducting nanowire single-photon detectors," IEEE Trans. Appl. Supercond. **17**, 581–585 (2007).

[66]A. Dane, J. Allmaras, D. Zhu, M. Onen, M. Colangelo, R. Baghdadi, J.-L. Tambasco, Y. Morimoto, I. E. Forno, I. Charaev, Q. Zhao, M. Skvortsov, A. Kozorezov, and K. K. Berggren, "Self-heating hotspots in superconducting nanowires cooled by phonon black-body radiation," Nat. Commun. **13**, 5429 (2022).
[67]A. Stockhausen, K. Il'in, M. Siegel, U. Södervall, P. Jedrasik, A. Semenov, and H.-W. Hübers, "Adjustment of self-heating in long superconducting thin film NbN microbridges," Supercond. Sci. Technol. **25**, 035012 (2012).
[68]M. Sidorova, A. D. Semenov, H.-W. Hübers, S. Gyger, and S. Steinhauer, "Phonon heat capacity and self-heating normal domains in NbTiN nanostrips," Supercond. Sci. Technol. **35**, 105005 (2022).
[69]T. Xu, S. Chen, H. K. Shi, X. Q. Jia, L. B. Zhang, Q. Y. Zhao, X. C. Tu, L. Kang, J. Chen, and P. H. Wu, "Effect of buffer layer on thermal recovery of superconducting nanowire single-photon detector," Supercond. Sci. Technol. **34**, 074002 (2021).
[70]G.-z. Xu, W.-j. Zhang, L.-x. You, Y.-z. Wang, J.-m. Xiong, D.-H. Fan, L. Wu, H.-q. Yu, H. Li, and Z. Wang, "Millimeter-scale active area superconducting microstrip single-photon detector fabricated by ultraviolet photolithography," Opt. Express **31**, 16348 (2023).
[71]L. J. van der Pauw, "A method of measuring the resistivity and Hall coefficient on lamellae of arbitrary shape," Philips Tech. Rev. **20**, 220–224 (1958).
[72]I. Miccoli, F. Edler, H. Pfnür, and C. Tegenkamp, "The 100th anniversary of the four-point probe technique: The role of probe geometries in isotropic and anisotropic systems," J. Phys.: Condens. Matter **27**, 223201 (2015).
[73]Y. Ivry, C. S. Kim, A. E. Dane, D. De Fazio, A. N. McCaughan, K. A. Sunter, Q. Zhao, and K. K. Berggren, "Universal scaling of the critical temperature for thin films near the superconducting-to-insulating transition," Phys. Rev. B **90**, 214515 (2014).
[74]B. L. Zink, R. Pietri, and F. Hellman, "Thermal conductivity and specific heat of thin-film amorphous silicon," Phys. Rev. Lett. **96**, 055902 (2006).
[75]J. C. Thompson and B. A. Younglove, "Thermal conductivity of silicon at low temperatures," J. Phys. Chem. Solids **20**, 146–149 (1961).
[76]A. J. Kerman, D. Rosenberg, R. J. Molnar, and E. A. Dauler, "Readout of superconducting nanowire single-photon detectors at high count rates," J. Appl. Phys. **113**, 144511 (2013).
[77]G.-Z. Xu, W.-J. Zhang, L.-X. You, J.-M. Xiong, X.-Q. Sun, H. Huang, X. Ou, Y.-M. Pan, C.-L. Lv, H. Li, Z. Wang, and X.-M. Xie, "Superconducting microstrip single-photon detector with system detection efficiency over 90% at 1550 nm," Photonics Res. **9**, 958 (2021).
[78]A. G. Kozorezov, C. Lambert, F. Marsili, M. J. Stevens, V. B. Verma, J. P. Allmaras, M. D. Shaw, R. P. Mirin, and S. W. Nam, "Fano fluctuations in superconducting-nanowire single-photon detectors," Phys. Rev. B **96**, 054507 (2017).